Quantification of Mixed Bloch-Néel Topological Spin Textures Stabilized by the Dzyaloshinskii-Moriya Interaction in Co/Pd Multilayers

Joseph A. Garlow, Shawn D. Pollard, Marco Beleggia, Tanmay Dutta, Hyunsoo Yang, and Yimei Zhu

Phys. Rev. Lett. **122**, 237201 — Published 10 June 2019

DOI: 10.1103/PhysRevLett.122.237201

Quantification of mixed Bloch/Néel topological spin textures stabilized by the Dzyaloshinskii–Moriya interaction in Co/Pd multilayers

Joseph A. Garlow[1,2], Shawn D. Pollard[3], Marco Beleggia[4], Tanmay Dutta[3], Hyunsoo Yang[3], Yimei Zhu[1,2*]

[1] Condensed Matter Physics and Materials Science Division, Brookhaven National Laboratory, Upton, NY 11973 USA

[2] Department of Materials Science and Chemical Engineering, Stony Brook University, Stony Brook, NY, 11794, USA

[3] Department of Electrical and Computer Engineering, National University of Singapore, Singapore, 117576, Singapore

[4] DTU Nanolab, Technical University of Denmark, 2800 Kgs. Lyngby, Denmark

The three-dimensional structure of nanoscale topological spin textures stabilized by the Dzyaloshinskii-Moriya interaction is governed by the delicate competition between the exchange, demagnetization and anisotropy energies. The quantification of such spin textures through direct experimental methods is crucial towards understanding the fundamental physics associated with their ordering, as well as their manipulation in spintronic devices. Here, we extend the Lorentz transmission electron microscopy technique to quantify mixed Bloch/Néel chiral spin textures stabilized by the Dzyaloshinskii-Moriya interaction in Co/Pd multilayers. Analysis of the observed intensities under varied imaging conditions coupled to corroborative micromagnetic simulations yield vital parameters that dictate the stability and properties of the complex spin texture, namely the degree of mixed Bloch/Néel character, the domain wall width, the strength of the Dzyaloshinskii-Moriya interaction and the exchange stiffness. This approach provides the necessary framework for application of quantitative Lorentz phase microscopy to a broad array of topological spin systems.

Chiral spin configurations such as homochiral Néel walls [1,2] and skyrmions [3–7] have garnered intense interest recently for next-generation magnetic-based memory, logic, and sensor

applications [8–11]. These spin textures are typically a result of the Dzyaloshinskii-Moriya interaction (DMI), an asymmetric exchange interaction that breaks the energy degeneracy between the two possible chiralities [12,13]. In a heavy metal/ferromagnetic system with perpendicular magnetic anisotropy (PMA), the DMI results from spin-orbit coupling at the interface. In thick PMA films with DMI, the exchange and DMI energies favor Bloch and Néel walls, respectively, while the demagnetization energy favors a twisted magnetization that minimizes stray fields [14]. The competition between these energies can lead to complex domain walls that cannot be described as fully Bloch or Néel [15–17], in addition to stabilizing exotic spin topologies such as chiral bobbers [18,19], and plays an essential role in the dynamics of chiral domain walls. Specifically, it influences domain wall velocities [20], how they interact with defects [21], and, for the case of skyrmions, modifies their Hall angle [16] where, with ideal Bloch/Néel mixing, a skyrmion Hall angle of zero can be obtained [22]. Thus, understanding this energy balance is required for the development of spintronic devices based on chiral domain walls. The energy terms are characterized by the exchange stiffness, A_{ex}, the DMI constant, $\boldsymbol{D}$, and the saturation magnetization, M_s, which can be extracted from precise measurements of the domain wall spin texture given the strength of the uniaxial anisotropy, K_u, that may be measured using magnetometry techniques. Recently, Legrand *et al.* [16] and Dovzhenko *et al.* [17] demonstrated X-ray resonant magnetic scattering and nitrogen-vacancy magnetometry as methods to determine the surface structure of domain walls, and estimated the thickness dependence of the domain wall structure resulting from dipolar and DMI effective fields through comparison of a variety of samples. Yet, both techniques are restricted to deduce the domain wall structure from surface states and are unable to measure the domain wall width due to resolution limitations, which would provide a direct method to determine the strength of the exchange energy in such films. Therefore, these methods necessitate multiple experimental techniques to quantify the complete domain wall structure.

Full quantification of the complex three-dimensional spin topography across an individual domain wall remains an open challenge. Its resolution is key to facilitate spintronic technologies such as spin Hall/torque-based devices capable of manipulating spin textures [23], where chiral domain structures play the role of basic information carriers. Lorentz transmission electron microscopy (LTEM) is a classic tool to study magnetism [24–28] and has been successfully applied to understand the local spin order in materials capable of hosting magnetic skyrmions [4,5,29,30] and other chiral spin textures [1]. LTEM is directly sensitive to changes in magnetization for electron transparent thin films and, with precise control of experimental variables in conjunction with image simulations, can provide quantitative information on magnetic domain walls [31–33]. Here, we use LTEM to quantify the mixed-character of magnetic domain walls in an MgO (2 nm)/Pt (4 nm)/Co (0.7 nm)/[Pd (0.5 nm)/Co (0.7 nm)]$_{10}$/Pt (4 nm) stack with a strong DMI [29,34], where 10 is the repetition number of the Pd/Co bilayers (Fig. 1(a), inset) [35]. Through systematic fitting of the domain wall intensity profile as a function of sample tilt under identical imaging conditions with image simulations, we simultaneously measure the domain wall width, w, and the Bloch/Néel mixed-character parameter, η, defined as the thickness-averaged angle of the plane where spins rotate as they transition from the "up" to the "down" state: η=0°/90° corresponds to a Bloch/Néel wall, respectively. Pairing our results to micromagnetic simulations enables determination of the DMI strength and the exchange stiffness.

LTEM is based on the phase shift of the electron wave after crossing the local magnetic flux of a thin film sample. Magnetic contrast is observed when the sample is imaged out-of-focus, where the contrast is proportional to the curl of the magnetization in the small defocus limit (SDL) [36]. Here, we term Lorentz contrast as the SDL intensity profile that directly corresponds to the magnetization curl, while we term Fresnel contrast as the image intensity generated outside the SDL where interference effects are non-negligible. Fig. 1(a) shows the magnetization hysteresis loop of the sample studied using

vibrating sample magnetometry (VSM), while Fig. 1(b-d) display the spin texture as a function of applied field along the marked regions of the hysteresis. With an applied field of 11 mT (Fig. 1(b)), the magnetic state appears dense with a localized fine structure that varies at the scale of ~10 nm. As the magnetic field is increased, the spin texture becomes coarser such that narrow magnetic domains with a complex wall structure become apparent. At the applied field of 195 mT (Fig. 1(d)), the predominant spin structures are skyrmion-like near30 nm in size. The chirality of the Bloch component for the skyrmion-like textures highlighted in Fig. 1(d) can be of either sign, as indicated by their opposite contrast and by the line profiles in Fig. 1(h).

For magnetic domain walls with a mixed Bloch/Néel structure, there will be significant changes to the LTEM intensity when the sample is tilted, depending on the orientation of the wall with respect to the tilt axis. Upon lowering the applied field from saturation, isolated domains that can be analyzed appear (Fig. 1(e,f)). Line scans acquired from raw data shown in Fig. 1(g) reveal an asymmetric change in the contrast profile by tilting the sample. The profile at tilt appears mostly Néel-like, with only small Bloch contributions. This is a clear indication of a mixed-character domain wall and motivates analysis of the tilt dependent contrast to quantify the degree of mixing.

In a multilayer thin film with PMA, the magnetization unit vector of a mixed-character domain wall is typically expressed as:

$$\frac{\boldsymbol{M}}{M_s} = \left\{ \sin(\eta)\,\mathrm{sech}\left(\frac{x}{w}\right), \cos(\eta)\,\mathrm{sech}\left(\frac{x}{w}\right), \tanh\left(\frac{x}{w}\right) \right\}, \tag{1}$$

where M_s is the saturation magnetization of the thin film, w is the domain wall width, and η is the mixed-character parameter [37]. Although w and η may vary through the sample thickness, we consider them as thickness-averaged quantities. When the defocus is within the SDL, the normalized

"Lorentz" image intensity of a mixed-character wall oriented perpendicular to the tilt axis can be calculated analytically (see Supplementary Material for details):

$$I(x,\theta,\eta,\Delta)=1-\frac{L\Delta}{w}\operatorname{sech}\left(\frac{x}{w}\right)\left[\cos(\eta)\tanh\left(\frac{x}{w}\right)+\tan(\theta)\operatorname{sech}\left(\frac{x}{w}\right)\right], \quad (2)$$

where $L=\frac{B_0 t\lambda}{2\phi_0}$, $B_0=\mu_0 M_0$, t is the thickness of magnetic material, λ is the electron wavelength, Δ is the defocus value, $\phi_0=2.07\times10^{-15}\,\mathrm{Tm}^2$ is the flux quantum, and θ is the sample tilt angle. The validity of equation (2) is restricted to defocus values small enough to ensure that the Fresnel number corresponding to our experimental setup is larger than unity, i.e. $F=w^2/\lambda\Delta>1$ and, therefore, $\Delta<w^2/\lambda\sim40$ μm.

The calculated Lorentz intensities of Néel, Bloch and mixed domain walls using Eq. (2) are shown in Fig. 2(a-c). At $\theta=0^\circ$, Néel walls do not generate contrast, while Bloch walls generate symmetric bright/dark contrast according to their chirality. Mixed domain walls display Lorentz contrast analogous to that of Bloch walls with a reduced intensity proportional to the $\cos(\eta)$ factor in Eq. (2). As a magnetic domain wall is tilted along an axis perpendicular to its length, its contrast is modified by the projection of the domain wall itself and the projection of the out-of-plane magnetization with respect to the tilt axis, in addition to the change in the projected sample thickness.

The observed broadening of the domain wall contrast with defocus shown in Supplemental Fig. 3 [35] highlights the inadequacy of Eq. (2) when applied beyond the SDL: the role of Δ in Eq. (2) is limited to a linear change in contrast, and does not influence w and η. However, the exact calculation of the image intensity beyond the SDL requires the full Fresnel propagator describing how an electron

wavefront evolves in free space. While mathematically and numerically straightforward using standard image formation theory, the lack of an analytical solution prevents the use of Fresnel intensities as model functions for fitting the data. A comparison between the calculated Lorentz and Fresnel contrast profiles at varying defocus, shown in Fig. 2(d), reveals that the former fails to capture the natural spreading of the wavefront and it over-/underestimates the intensity values of minima/maxima, respectively. Consequently, fitting an experimental Fresnel image (Fig. 2(e)) with the Lorentz formula in Eq. (2) results in an apparent enlargement of the wall width as a function of defocus, and in significant uncertainties for the estimation of L, w, and η. This is illustrated in Fig. 2(f), where the Lorentz-fit Fresnel intensities corresponding to a *w*=10 nm, η=60° domain wall observed in the $\pm$1 mm defocus range results in the apparent non-linear increase of *w* up to 20-25 nm (blue curve), and in fluctuations in η up to a few degrees (red curve). Our strategy to account for these issues is to: 1) fit each intensity profile at a given Δ and θ using Eq. (2) as a model function with *w* and η as free parameters, and 2) extrapolate the resulting trends of *w* and η with defocus using the correct Fresnel intensities, calculated as shown in the Supplementary Material and represented by the curves shown in Fig. 2(f).

The determination of η is achieved by fitting Eq. (2) for w simultaneously with a global fit to η over a set of images acquired at a constant defocus for sample tilts from -30° to 30° in increments of 10° (Fig. 3). The effect of sample tilt on the projected spin structure is visualized in Fig. 3(a) where a mixed skyrmion ($\eta = 62^\circ$) is displayed at 0°, 30° and 45° tilt angles. Corresponding images of two magnetic domains with regions oriented orthogonal to the tilt axis are highlighted by the red box in Fig. 3(b) while a complete set of images acquired at each tilt can be seen in Supplemental Fig. 2 for 737 μm defocus [35]. All fitting for the determination of η and w is presented in Fig. 3(c). The η values measured by fitting with Eq. (2) (red data points) as a function of defocus are displayed in Fig. 3(d) and specify an η

value around 60° that is consistent across tilt and defocus. Extrapolation of the measured values using Fresnel intensity simulations gives a value of $\eta = 56^\circ \pm 5^\circ$, where the uncertainty is estimated from the spread of fit η values for individually fit line scans. Similarly, the width parameter is determined as $w = 10 \pm 2$ nm. Further details regarding the influence in-plane fields have on the extraction of η are discussed in the Supplementary Materials [35].

An estimate for $\boldsymbol{D}$ and A_{ex} is obtained by matching the experimental values of η and w to micromagnetics. Simulations were carried out using MuMax3 [38] with a cell size of 2x2x 1 nm^3 on a 1024x1024x13 nm^3 structure with periodic boundary conditions. A Néel wall was initialized in the center running along the y-axis, and relaxed. We adopt the values $M_s = 880$ kA/m and $K_u = 0.61$ MJ/m^3 from the VSM measurements. $\boldsymbol{D}$ and A_{ex} were varied to demonstrate their effect on the domain wall width and on the deviation angle (Fig. 4(a-c)). We find that the domain wall width varies only weakly with DMI, while the width changes significantly with variation in A_{ex} (Fig. 4(b)). Matching the width with experimental results suggests an exchange stiffness between 23–30 pJ/m, similar to that of bulk Co and expected for Co/Pd multilayers with an ultrathin Pd spacer [39]. However, η varies significantly with both A_{ex} and $\boldsymbol{D}$ (Fig. 4(a, c)). Using an exchange stiffness in agreement with the measured w provides a value of $\boldsymbol{D}$ in the range 1.0–1.1 mJ/m^2. This value is consistent with recent reports suggesting large values of $\boldsymbol{D}$ in Pd based systems [34]. Our findings align with previous results of Co/Pt symmetric multilayers [40], with a possible origin of the DMI being inequivalent Pd/Co and Co/Pd interfaces [34,41,42]. The large dependency of η with both $\boldsymbol{D}$ and A_{ex} further confirms the need for a robust technique to make quantitative measurements of the physical parameters governing chiral domain structures. This technique may be broadly applied to other systems with strong DMI and/or complex material profiles that pose challenges for the measurement of exchange stiffness.

We developed a quantitative Lorentz microscopy framework to measure the vital parameters of mixed Bloch/Néel domain walls in a model Co/Pd multilayer. Using the derived equation for Lorentz intensity from electron phase shifts, we measure the degree of Bloch/Néel mixed-character ($\eta = 56^\circ \pm 5^\circ$) and the domain wall width ($w = 10 \pm 2$ nm) through tilt- and defocus-dependent contrast analysis. Coupling the results to micromagnetic simulations confines the magnitude of the exchange stiffness to 23–30 pJ/m and the strength of the DMI to 1.0–1.1 mJ/m^2, revealing the energy balance underpinning the complex spin structure. Direct determination of the relevant energy terms from a single experiment constitutes a substantial advance in understanding the physics that governs magnetic order in topological systems with a strong DMI, towards spintronic applications based on chiral magnetism.

Acknowledgements:

This research was supported by US Department of Energy, Office of Basic Energy Sciences, Division of Materials Science and Engineering, under Contract No. DE-SC0012704 and the National Research Foundation (NRF), Prime Minister's Office, Singapore, under its Competitive Research Programme (CRP award no. NRFCRP12-2013-01).

J.A.G., S.D.P. and M.B. contributed equally to this work.

*zhu@bnl.gov

References:

[1] M. J. Benitez, A. Hrabec, A. P. Mihai, T. A. Moore, G. Burnell, D. Mcgrouther, C. H. Marrows, and S. McVitie, Nat. Commun. **6**, 8957 (2015).

[2] M. Bode, M. Heide, K. Von Bergmann, P. Ferriani, S. Heinze, G. Bihlmayer, A. Kubetzka, O. Pietzsch, S. Blügel, and R. Wiesendanger, Nature **447**, 190 (2007).

[3] X. Z. Yu, Y. Onose, N. Kanazawa, J. H. Park, J. H. Han, Y. Matsui, N. Nagaosa, and Y. Tokura, Nature **465**, 901 (2010).

[4] A. Tonomura, X. Yu, K. Yanagisawa, T. Matsuda, Y. Onose, N. Kanazawa, H. S. Park, and Y. Tokura, Nano Lett. **12**, 1673 (2012).

[5] S. Seki, X. Z. Yu, S. Ishiwata, and Y. Tokura, Science **336**, 198 (2012).

[6] U. K. Rößler, A. N. Bogdanov, and C. Pfleiderer, Nature **442**, 797 (2006).

[7] R. Wiesendanger, Nat. Rev. Mater. **1**, 16044 (2016).

[8] A. Fert, V. Cros, and J. Sampaio, Nat. Nanotechnol. **8**, 152 (2013).

[9] A. Fert, N. Reyren, and V. Cros, Nat. Rev. Mater. **2**, 17031 (2017).

[10] R. Tomasello, E. Martinez, R. Zivieri, L. Torres, M. Carpentieri, and G. Finocchio, Sci. Rep. **4**, 6784 (2015).

[11] W. Jiang, G. Chen, K. Liu, J. Zang, S. G. E. te Velthuis, and A. Hoffmann, Phys. Rep. **704**, 1 (2017).

[12] I. Dzyaloshinsky, J. Phys. Chem. Solids **4**, 241 (1958).

[13] T. Moriya, Phys. Rev. Lett. **4**, 4 (1960).

[14] S. A. Montoya, S. Couture, J. J. Chess, J. C. T. Lee, N. Kent, D. Henze, S. K. Sinha, M.-Y. Im, S. D. Kevan, P. Fischer, B. J. McMorran, V. Lomakin, S. Roy, and E. E. Fullerton, Phys. Rev. B **95**, 024415 (2017).

[15] J. Y. Chauleau, W. Legrand, N. Reyren, D. Maccariello, S. Collin, H. Popescu, K. Bouzehouane, V. Cros, N. Jaouen, and A. Fert, Phys. Rev. Lett. **120**, 037202 (2018).

[16] W. Legrand, J.-Y. Chauleau, D. Maccariello, N. Reyren, S. Collin, K. Bouzehouane, N. Jaouen, V. Cros, and A. Fert, Sci. Adv. **4**, eaat0415 (2018).

[17] Y. Dovzhenko, F. Casola, S. Schlotter, T. X. Zhou, F. Büttner, R. L. Walsworth, G. S. D. Beach, and A. Yacoby, Nat. Commun. **9**, 2712 (2018).

[18] F. Zheng, F. N. Rybakov, A. B. Borisov, D. Song, S. Wang, Z.-A. Li, H. Du, N. S. Kiselev, J. Caron, A.

Kovács, M. Tian, Y. Zhang, S. Blügel, and R. E. Dunin-Borkowski, Nat. Nanotechnol. **13**, 451 (2018).

[19] A. S. Ahmed, J. Rowland, B. D. Esser, S. R. Dunsiger, D. W. McComb, M. Randeria, and R. K. Kawakami, Phys. Rev. Mater. **2**, 041401 (2018).

[20] Y. Yoshimura, K.-J. Kim, T. Taniguchi, T. Tono, K. Ueda, R. Hiramatsu, T. Moriyama, K. Yamada, Y. Nakatani, and T. Ono, Nat. Phys. **12**, 157 (2016).

[21] K. Sato and O. A. Tretiakov, Appl. Phys. Lett. **108**, 122403 (2016).

[22] K.-W. Kim, K.-W. Moon, N. Kerber, J. Nothhelfer, and K. Everschor-Sitte, Phys. Rev. B **97**, 224427 (2018).

[23] D. Maccariello, W. Legrand, N. Reyren, K. Garcia, K. Bouzehouane, S. Collin, V. Cros, and A. Fert, Nat. Nanotechnol. **13**, 233 (2018).

[24] P. Grundy, D. Hothersall, G. Jones, B. Middleton, and R. Tebble, IEEE Trans. Magn. **7**, 483 (1971).

[25] P. J. Grundy and S. R. Herd, Phys. Status Solidi **20**, 295 (1973).

[26] S. R. Herd and P. Chaudhari, Phys. Status Solidi **18**, 603 (1973).

[27] S. R. Herd, Phys. Status Solidi **38**, 305 (1976).

[28] T. Suzuki and M. Takahashi, Jpn. J. Appl. Phys. **17**, 1371 (1978).

[29] S. D. Pollard, J. A. Garlow, J. Yu, Z. Wang, Y. Zhu, and H. Yang, Nat. Commun. **8**, 14761 (2017).

[30] J. J. Chess, S. A. Montoya, E. E. Fullerton, and B. J. McMorran, AIP Adv. **7**, 056807 (2017).

[31] H. Gong and J. N. Chapman, J. Magn. Magn. Mater. **67**, 4 (1987).

[32] S. J. Lloyd, J. C. Loudon, and P. A. Midgley, J. Microsc. **207**, 118 (2002).

[33] R. H. Wade, Proc. Phys. Soc. **79**, 1237 (1962).

[34] A. V. Davydenko, A. G. Kozlov, A. G. Kolesnikov, M. E. Stebliy, G. S. Suslin, Y. E. Vekovshinin, A. V. Sadovnikov, and S. A. Nikitov, Phys. Rev. B **99**, 014433 (2019).

[35] See Supplemental Material at [URL will be inserted by publisher] for further details regarding Eq. (2) and additional imaging and analysis in the Figures, which includes Refs. [34, 43-50].

[36] M. Beleggia, M. A. Schofield, V. V. Volkov, and Y. Zhu, Ultramicroscopy **102**, 37 (2004).

[37] I. Lemesh, F. Büttner, and G. S. D. Beach, Phys. Rev. B **95**, 174423 (2017).

[38] A. Vansteenkiste, J. Leliaert, M. Dvornik, M. Helsen, F. Garcia-Sanchez, and B. Van Waeyenberge, AIP Adv. **4**, 107133 (2014).

[39] V. Kamberský, P. de Haan, J. Šimšová, S. Porthun, R. Gemperle, and J. C. Lodder, J. Magn. Magn. Mater. **157–158**, 301 (1996).

[40] S.-G. Je, D.-H. Kim, S.-C. Yoo, B.-C. Min, K.-J. Lee, and S.-B. Choe, Phys. Rev. B **88**, 214401 (2013).

[41] H. Awano, Y. Suzuki, T. Katayama, and A. Itoh, J. Appl. Phys. **68**, 4569 (1990).

[42] D.-O. Kim, K. M. Song, Y. Choi, B.-C. Min, J.-S. Kim, J. W. Choi, and D. R. Lee, Sci. Rep. **6**, 25391 (2016).

[43] F. J. A. den Broeder, H. C. Donkersloot, H. J. G. Draaisma, and W. J. M. de Jonge, J. Appl. Phys. **61**, 4317 (1987).

[44] J. W. Lau, M. A. Schofield, and Y. Zhu, Ultramicroscopy **107**, 396 (2007).

[45] M. A. Schofield, M. Beleggia, Y. Zhu, and G. Pozzi, Ultramicroscopy **108**, 625 (2008).

[46] D. B. Williams and C. B. Carter, *Transmission Electron Microscopy: A Textbook for Materials Science* (Springer US, 2009).

[47] E. Völkl, L. F. Allard, and D. C. Joy, *Introduction to Electron Holography* (Springer US, 1999).

[48] M. Born and E. Wolf, *Principles of Optics: Electromagnetic Theory of Propagation, Interference and Diffraction of Light* (Cambridge University Press, 1999).

[49] C. T. Koch, Micron **63**, 69 (2014).

[50] S. Bajt, A. Barty, K. Nugent, M. McCartney, M. Wall, and D. Paganin, Ultramicroscopy **83**, 67 (2000).

Figure Captions:

Figure 1: (a) Co/Pd magnetic hysteresis measured with VSM. The insets show schematics of the sample geometry and the interfacial DMI. (b-d) LTEM images of the sample as a function of applied fields. (e) 180° domain walls appearing at low applied fields with a decreased density. (f) The same region as in (e) after tilting the sample 30° around the tilt axis shown. (g) Line scans from the magenta and green boxes in (e,f) demonstrate asymmetric LTEM contrast at tilt, suggesting mixed-character domain walls. (h) Line scans from the regions highlighted in (d) reveal skyrmion-like structures with opposing Bloch components. The scale bar for all images is 1 μm.

Figure 2: (a-c) Calculated intensity profile for Néel, Bloch and mixed domain walls as a function of tilt using Eq. (2). For (c), the mixed-character parameter, η, equals 60°. A schematic of a mixed domain wall is shown with the inset. (d) Fresnel and Lorentz intensities of a 10 nm mixed wall ($\eta = 45^\circ$, $\theta = -30^\circ$) as a function of defocus. (e) Line scans of the Fresnel (brown), Lorentz (blue) and best-fit Lorentz profile to the Fresnel (green) intensities at 0.75mm defocus. At this defocus, the 10 nm wall is Lorentz-fit as a 19 nm wall, laterally shifted by 4.3 nm, and with a mixed-character parameter of 23°. (f) Curves representing the trends in the *w* (blue) and η (red) parameters as a function of defocus determined using Eq. (2) as a model function to fit Fresnel intensities. The asymmetry between over- and under-focus originates from interference effects with converging/diverging wavefronts, respectively.

Figure 3: (a) Influence of tilt on the projected spin texture in the plane perpendicular to the beam direction. The tilt axis is indicated in black. (b) Characteristic images of domains with mixed-character walls acquired at 0° and 30° tilt for a defocus of 737 μm. The areas for analysis are highlighted in blue from the red box and identify regions oriented orthogonal to the tilt axis. (c) Lorentz-fits across tilt with constant defocus. (d) Best-fits for both η (red) and w (blue). Fresnel-extrapolation to zero defocus determines the values, $\eta = 56^\circ \pm 5^\circ$ and $w = 10 \pm 2$ nm. The inset defines the η and w parameters used for fitting. The applied field is 25 mT for all images and the scale bars in (b) are 500 nm.

Figure 4: (a) Schematic domain wall profiles in the x-z plane as a function of DMI. The color represents the y-component of the magnetization. (b) Domain wall width as a function of exchange stiffness for various values of DMI. (c) Characteristic deviation angle as a function of exchange stiffness for various values of DMI. The shaded regions demark the experimentally measured regions.

Figure 1:

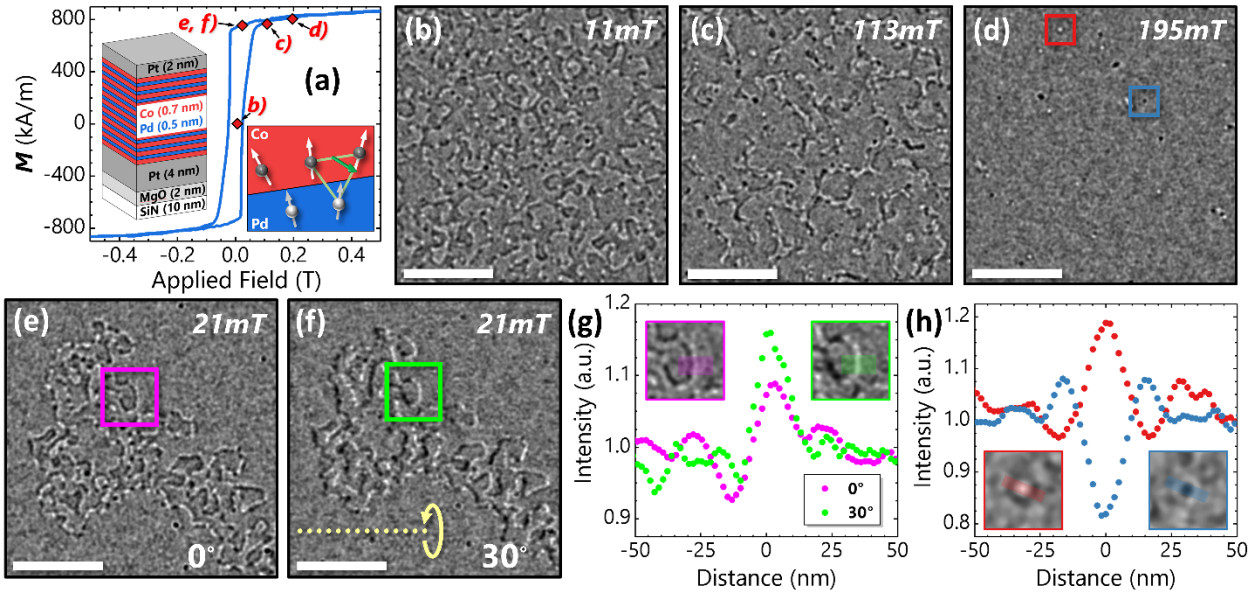
(a)
M (kA/m)
Applied Field (T)
Pt (2 nm)
Co (0.7 nm)
Pd (0.5 nm)
Pt (4 nm)
MgO (2 nm)
SiN (10 nm)
Co
Pd
e, f)
d)
c)
b)
(b) 11mT
(c) 113mT
(d) 195mT
(e) 21mT
0°
(f) 21mT
30°
(g)
Intensity (a.u.)
Distance (nm)
0°
30°
(h)
Intensity (a.u.)
Distance (nm)

Figure 2:

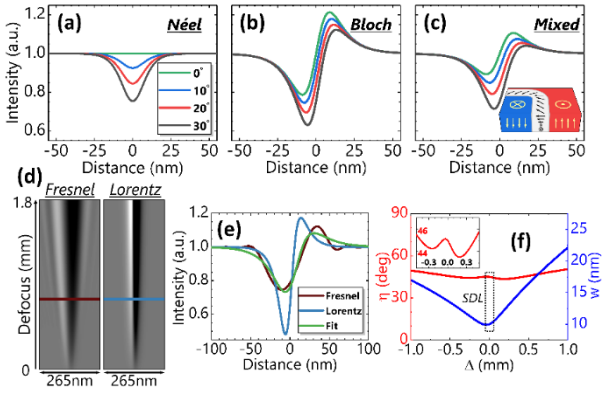
(a)
Néel
(b)
Bloch
(c)
Mixed
Intensity (a.u.)
Distance (nm)
0°
10°
20°
30°
(d)
Fresnel
Lorentz
Defocus (mm)
265nm
265nm
(e)
Fresnel
Lorentz
Fit
(f)
SDL
η (deg)
w (nm)
Δ (mm)

Figure 3:

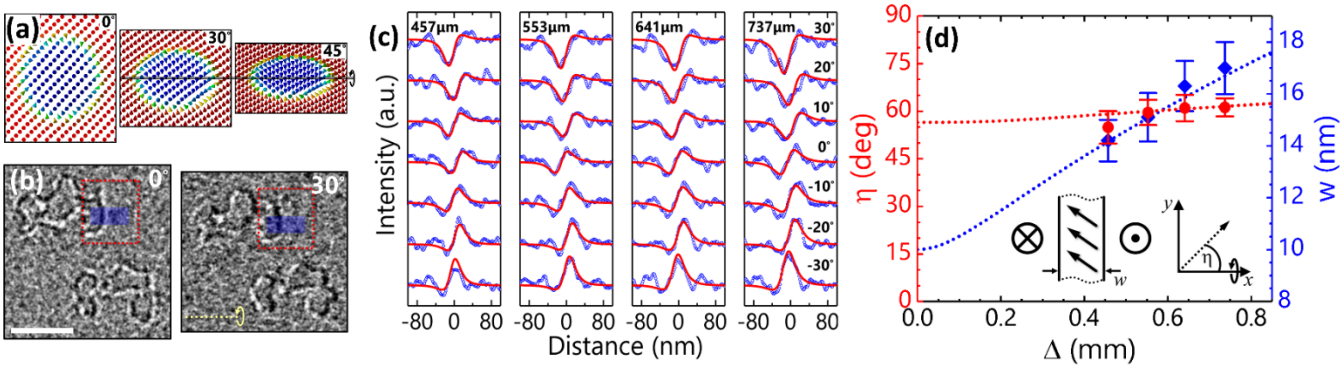
(a)
0°
30°
45°
(b)
0°
30°
(c)
457μm
553μm
641μm
737μm
30°
20°
10°
0°
-10°
-20°
-30°
Intensity (a.u.)
-80 0 80
Distance (nm)
(d)
η (deg)
w (nm)
Δ (mm)
0.0 0.2 0.4 0.6 0.8
0 15 30 45 60 75 90
8 10 12 14 16 18
y
x
η
w

Figure 4:

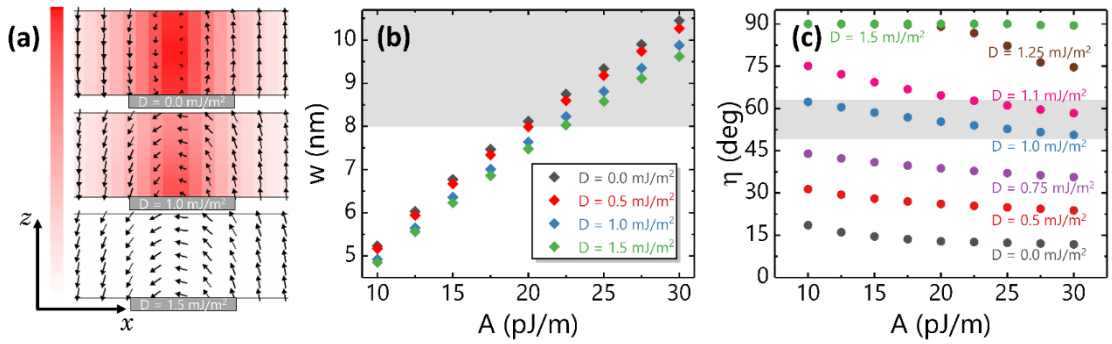
(a)
D = 0.0 mJ/m²
D = 1.0 mJ/m²
D = 1.5 mJ/m²
z
x
(b)
w (nm)
A (pJ/m)
D = 0.0 mJ/m²
D = 0.5 mJ/m²
D = 1.0 mJ/m²
D = 1.5 mJ/m²
(c)
η (deg)
A (pJ/m)
D = 1.5 mJ/m²
D = 1.25 mJ/m²
D = 1.1 mJ/m²
D = 1.0 mJ/m²
D = 0.75 mJ/m²
D = 0.5 mJ/m²
D = 0.0 mJ/m²